Next Materials 12 (2026) 102149

Contents lists available at ScienceDirect

Next Materials

journal homepage: www.sciencedirect.com/journal/next-materials

Research article

Coordination-driven structural evolution of flumequine with transition metals, molecular docking and its biological implications

Gehan S. Elasala, Alaa E. Ali, Y. Sh. Mahrouse, Marwa H. Eldeeb *, Rana M. Atta

Department of Chemistry, Faculty of Science, Damanhur University, Egypt

ARTICLE INFO

Keywords:
Flumequine
Metal coordination
Spectral characterization
Solid-state structure
Biological evaluation
Molecular docking

ABSTRACT

The coordination chemistry of flumequine was investigated through the synthesis of a series of transition metal complexes with Mn(II), Co(II), Ni(II), Cu(II), Zn(II), Cr(III), Hg(II), and Cd(II) ions in a 1:2 metal-to-ligand ratio. Infrared spectral data ($\Delta\nu \approx 195–213\ cm^{-1}$) indicated coordination of the ligand through the carbonyl and carboxylate oxygen atoms. The structures of the synthesized complexes were characterized using elemental analysis, infrared spectroscopy, electronic spectra, magnetic measurements, and molar conductivity studies. The combined data suggests a proposed octahedral geometry around the metal ions. The molar conductance values in dimethyl sulfoxide (DMSO, 10^{-3} M) indicate a non-electrolytic nature for all complexes. Thermal analysis (TGA/DSC/DTA) revealed multistep decomposition patterns terminating in metal oxide residues. Powder X-ray diffraction suggested the crystalline nature of Zn and Hg complexes, with calculated average crystalline size 10.85 ± 1.18 and 12.65 ± 1.15 nm respectively, while SEM analysis showed distinct morphological variations upon metal coordination. Antimicrobial and antifungal screening against *Staphylococcus aureus, Bacillus subtilis, Escherichia coli, Pseudomonas aeruginosa,* and *Candida albicans* revealed variations in inhibition zone diameters (15–30 mm) among the complexes. Based on docking analysis flumequine and its corresponding metal complexes showed different binding affinities toward DNA gyrase (PDB ID: 4Z2C). The Zn(II)–flumequine complex showed the most favorable binding energy (−13.0 kcal/mol) compared with flumequine and other complexes. Overall, the results demonstrate that metal coordination modulates the physicochemical and biological properties of flumequine.

1. Introduction

Fluoroquinolone antibiotics constitute an important class of synthetic antimicrobial agents that continue to attract scientific interest owing to their broad-spectrum bactericidal activity [1]. Their mechanism of action is primarily associated with the inhibition of bacterial DNA gyrase and topoisomerase IV, enzymes essential for DNA replication and transcription. Members of this class generally exhibit high efficacy against Gram-negative bacteria, whereas their activity against Gram-positive organisms is more variable and has been increasingly challenged by the emergence of resistant strains, including methicillin-resistant *Staphylococcus aureus* [2]. In addition, several fluoroquinolones demonstrate activity against atypical pathogens such as *Mycobacterium*, *Chlamydia*, and *Mycoplasma*, while their effectiveness against anaerobic bacteria remains limited [3]. Flumequine is a first-generation synthetic fluoroquinolone that was initially introduced for the treatment of bacterial infections [4]. Despite its early clinical application, flumequine was subsequently withdrawn from routine human use, and its marketing authorization was revoked in several regions, including the European Union, mainly due to limited systemic bioavailability and unfavorable pharmacokinetic properties. The antibacterial activity of flumequine is attributed to its ability to interfere with DNA-unwinding enzymes, thereby inhibiting bacterial DNA replication. Beyond human medicine, flumequine found restricted application in veterinary practice, where it was employed for the treatment of enteric infections in livestock and aquaculture, albeit within limited regulatory frameworks and geographic regions [5–9]. The IUPAC name of flumequine is 9-Fluoro-6,7-dihydro-5-methyl-1-oxo-1H,5H-benzo [ij]-quinolizine-2-carboxylic acid. The molecular formula is $C_{14}H_{12}FNO_3$, Fig. 1.

Previous studies have extensively explored the coordination chemistry of flumequine with various transition metal ions, particularly Mn (II), Ni(II), and Zn(II), mainly through the formation of mixed-ligand complexes. In these systems, flumequine typically acts as a bidentate

* Corresponding author.
E-mail address: Marwa-Hussein@sci.dmu.edu.eg (M.H. Eldeeb).

https://doi.org/10.1016/j.nxmate.2026.102149
Received 1 March 2026; Received in revised form 11 April 2026; Accepted 23 April 2026
Available online 30 April 2026

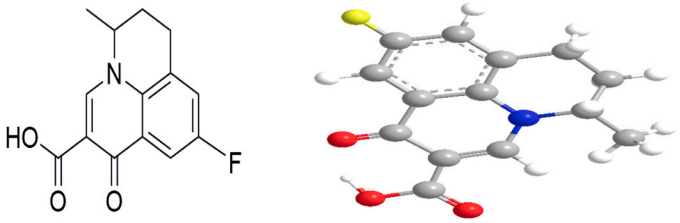

Fig. 1. 2D and 3D structure of flumequine.

ligand coordinating via the carboxylate and pyridone oxygen atoms, while additional nitrogen-donor co-ligands such as 1,10-phenanthroline, 2,2′-bipyridine, and pyridine are frequently incorporated. These studies have primarily focused on structural characterization, along with biological evaluations including antimicrobial activity and interactions with biomolecules such as DNA and serum albumins [10–12]. In addition, organotin(IV) complexes of flumequine have been reported, where various organotin moieties were coordinated to the ligand without the use of classical nitrogen donor co-ligands. These complexes were mainly investigated in terms of their antimicrobial, antifungal, and DNA-binding properties [13]. More recently, lanthanide complexes involving metals such as lanthanum(III), samarium(III), and terbium(III) have been synthesized, with emphasis on structural characterization and biological activity, particularly anticancer properties [14]. Overall, most of the reported studies have primarily focused on the structural characterization and biological evaluation of flumequine metal complexes, particularly in mixed-ligand systems. However, comparatively limited attention has been given to comprehensive investigations that combine thermal analysis, ESR studies, and molecular docking. In this context, the present study aims to explore the coordination behavior of flumequine with selected metal ions and to provide a detailed investigation of its physicochemical and biological properties. Special emphasis is placed on the use of flumequine as a ligand, which has not been extensively explored in previous studies, in addition to evaluating the effect of metal complexation on its biological activity.

2. Experimental

2.1. Materials and reagents

All chemicals and reagents employed in this study were of analytical grade and were used as received without further purification. Flumequine was obtained from a commercial source and served as the primary ligand precursor. Metal precursors used were ($MnCl_2.4H_2O$), ($CoCl_2.6H_2O$), ($NiCl_2.6H_2O$), ($CuCl_2.6H_2O$), ($ZnCl_2$), ($CrCl_3.6H_2O$), ($HgCl_2$), and ($CdCl_2$) that used as metal sources for complex formation. Common solvents such as ethanol, methanol, DMSO and distilled water were utilized throughout the synthesis and purification procedures.

2.2. Physical measurements and analytical techniques

Elemental composition analyses for carbon, hydrogen, nitrogen, and sulfur of the ligand and its corresponding metal complexes were carried out at the Central Laboratory, Cairo University, using a CHNS elemental analyzer [15]. The chloride ion content in the synthesized complexes was determined volumetrically by employing the standard Volhard titration procedure [16], the molar conductivity of the complexes was determined in DMSO as solvent at a concentration of 10^{-3} M using a HACH conductivity meter. All measurements were carried out at room temperature using freshly prepared solutions. Infrared spectral measurements were recorded over the range of 4000–400 cm^{-1} using KBr pellet techniques on a Fourier-transform infrared spectrometer [17,18]. Electronic absorption spectra of the solid samples were obtained in the form of Nujol mull dispersions using a UV–Visible spectrophotometer [19]. Magnetic susceptibility measurements were performed at room temperature utilizing the Faraday balance method, and the effective magnetic moments (μ_eff) were calculated from the experimentally corrected molar susceptibility values. Electron spin resonance (ESR) spectra were recorded in the X-band frequency range using a reflection-type spectrometer operating at approximately 9 GHz. Measurements were performed with a cylindrical resonant cavity, and field modulation was applied at a frequency of 100 kHz throughout the data collection process. The external magnetic field was precisely controlled using an LMR gaussmeter, while the g-factor values were determined by comparison with the standard DPPH reference signal. Thermal properties of the free ligand and the prepared metal complexes were examined using simultaneous thermogravimetric and differential thermal analysis. TGA, DTA, and DSC measurements were conducted from ambient temperature up to 800 °C at a constant heating rate of 20 °C min^{-1} under a continuous nitrogen atmosphere with a flow rate of 15 mL min^{-1}, employing platinum crucibles. The obtained thermal profiles were analyzed to elucidate the decomposition behavior and to estimate characteristic thermal transition parameters, including glass transition, melting, and crystallization temperatures. Powder X-ray diffraction measurements were carried out using Cu–Kα radiation (λ = 1.5406 Å) to investigate the crystalline nature and phase composition of the synthesized complexes [20,21]. Morphological characteristics and surface features were further examined by scanning electron microscopy [22].

2.3. Computer analysis programs

The molecular modeling calculations of the free ligands with Chem Bio Office 3D Ultra 11.0 and Avogadro programs. Applying Hyper chemistry computer program using PM3 semi empirical to measure charge density of the ligand.

2.4. Synthesis of metal complexes

The flumequine-based metal complexes were synthesized through a simple complexation procedure under controlled conditions. In typical preparation, flumequine (0.01 mol, 2.61 g) was dissolved in 40 mL of ethanol to obtain a clear ligand solution. Separately, the corresponding metal chlorides of Mn(II), Co(II), Ni(II), Cu(II), Zn(II), Cr(III), Hg(II), and Cd(II) (0.01 mol, calculated according to their molecular weights) were dissolved in 40 mL of ethanol. The metal salt solutions were added dropwise to the ligand solution under continuous stirring, maintaining equimolar amounts of metal and ligand (1:1 molar ratio) under continuous stirring. The reaction was carried out in a neutral medium, where the pH was monitored and remained around 7 without the addition of any external acid or base. The reaction mixture was gently heated for 2 h and then left overnight to ensure complete complexation. The resulting solid products were collected by filtration, washed several times with distilled water followed by methanol to remove any unreacted species, and finally dried under ambient conditions using vacuum desiccator over anhydrous $CaCl_2$.

2.5. Biological activity studies

The antimicrobial activity of the synthesized metal complexes was evaluated using the agar well diffusion technique following standard microbiological procedures [23,24]. Sterile nutrient agar (40 mL) was aseptically poured into sterile Petri dishes (15 cm diameter) to obtain a uniform agar layer with a thickness of approximately 4 mm. After solidification, the plates were incubated in an inverted position at 37 °C for 18 h to ensure proper surface drying. Microbial inoculum were prepared by subculturing the tested strains in 3 mL of sterile nutrient broth, and the turbidity of each suspension was adjusted to match the 0.5 McFarland standard (≈ 1×10^8 CFU mL^{-1}). The agar surfaces were uniformly inoculated using sterile cotton swabs to form a confluent microbial lawn. Wells of 8 mm diameter were aseptically punched into the agar, maintaining a minimum distance of 24 mm between adjacent wells. Each

well was loaded with 75 µL of the test compound, while dimethylformamide (DMF) was used as a negative control. The plates were kept at room temperature for 2 h to allow diffusion of the compounds, followed by incubation at 37 °C for 18–24 h. After incubation, the diameters of the inhibition zones were measured in three different directions, and the mean values were calculated. Antimicrobial activity was assessed against Gram-positive bacteria (*Staphylococcus aureus* ATCC 6538 P and *Bacillus subtilis* ATCC 19659), Gram-negative bacteria (*Escherichia coli* ATCC 8739 and *Pseudomonas aeruginosa* ATCC 9027), as well as the fungal strain *Candida albicans* ATCC 2091. Ciprofloxacin and clotrimazole were employed as reference drugs for antibacterial and antifungal activities, respectively.

2.6. Molecular docking studies

Molecular docking investigations were conducted using a dedicated computational workstation operating on a 64-bit system powered by an Intel® Core™ i5–4200U processor running at 2.10 GHz. Docking simulations were executed employing the Auto Dock Vina software package [25]. The three-dimensional crystallographic structure of the selected biological target (PDB ID: 4Z2C) was retrieved from the Protein Data Bank repository [26–28]. Prior to the docking process, the protein structure was pretreated using Auto Dock Tools to remove co-crystallized ligands and solvent molecules [29]. Polar hydrogen atoms were subsequently added, and Kollman united-atom charges were assigned to the receptor, while Gasteiger partial charges were applied to all ligand structures. The docking ligands included flumequine and its corresponding metal complexes, namely Co(II)–flu, Zn(II)–flu and Cu(II)–flu. Structural preparation and conversion of all ligands into the PDBQT file format were performed using the Open Babel graphical interface [30]. To ensure energetically favorable conformations, geometry optimization of the ligand molecules was carried out prior to docking using Avogadro software. Energy minimization was achieved through the conjugate gradient algorithm under the MMFF94 force field [31], allowing the generation of low-energy ligand structures suitable for docking analysis. Following the completion of docking simulations, the resulting binding modes were evaluated in terms of binding affinity, hydrogen bond formation, and amino acid interactions. Visualization and detailed inspection of the ligand–receptor complexes were performed using Discovery Studio Visualizer and PyMOL, enabling comprehensive interpretation of the molecular interactions governing binding behavior.

3. Results and discussion

3.1. Elemental analysis and composition

The elemental analysis results for carbon, hydrogen, nitrogen, and chlorine contents were found to be in good agreement with the proposed molecular formulas of the synthesized metal complexes. The obtained analytical data supported the formation of coordination compounds with a metal-to-ligand ratio of 1:2, confirming successful complexation between flumequine and the selected metal ions. The synthesized metal complexes were obtained as colored solids, with each complex exhibiting a distinct color depending on the metal ion. All complexes were found to be soluble in dimethyl sulfoxide (DMSO) and insoluble in water. The presence of chloride ions was confirmed using the Volhard method. Furthermore, molar conductivity measurements in DMSO (10^{-3} M) showed low values in the range of (8–17 Ω^{-1} cm^2 mol^{-1}), indicating that the complexes behave as non-electrolytes. This suggests that the chloride ions are coordinated to the metal center rather than existing as free counter ions, Table 1.

3.2. Infrared spectral analysis

Comparison between the FT-IR spectra of the free ligand and its metal complexes is essential to determine the coordination mode. Generally, coordination leads to a decrease in the bond force constant due to electron donation from the ligand to the metal center, resulting in a red shift. However, in some cases, a blue shift may occur due to partial electron donation from the metal to the ligand, which increases the bond order of the coordinated groups [32]. Infrared spectroscopy provided clear evidence for the coordination mode of flumequine within the synthesized metal complexes. The infrared spectrum of free flumequine exhibits a broad absorption band centered at 3383 cm^{-1} , which is assigned to the stretching vibration of OH group of carboxylic groups. In contrast, new broad bands appearing in the range of 3408–3452 cm^{-1} in the spectra of the complexes are attributed to the presence of water molecules [33], which are most likely coordinated to the metal centers. The incorporation of water molecules within the coordination sphere is further suggested from elemental and thermal analyses, as well as by the appearance of characteristic O–H stretching vibrations listed in Table 2, Fig.S.1. Additional confirmation of coordinated water is provided by the detection of metal–oxygen vibrational modes associated with rocking motions in the low-frequency region. The pyridone carbonyl stretching vibration (C═O) of free flumequine is observed at 1616 cm^{-1} .

Upon complexation, this band undergoes a noticeable shift toward higher frequencies, by 34–39 cm^{-1} in the spectra of the metal complexes. This shift reflects changes in the electronic environment of the pyridone

Table 1
Elemental analysis, formula, molar conductivities and colour of flumequine complexes.

Complexes	Colour	Λm Ω^{-1} cm^2 mol^{-1}	Calculated/(Found)%					
			C	H	N	M	Cl	F
[Cu(flu)$_2$(Cl)(H$_2$O)	Blue	14.7	52.65 (52.74)	3.70 (3.76)	4.28 (4.39)	9.78 (9.96)	5.51 (5.57)	5.60 (5.96)
[Co(flu)$_2$(Cl)(H$_2$O)]	Purple	10.3	53.12 (53.13)	3.76 (3.79)	4.40 (4.42)	9.26 (9.31)	5.52 (5.61)	6.05 (6.01)
[Ni(flu)$_2$Cl(H$_2$O)]	Green	8.1	53.10 (53.18)	3.74 (3.79)	4.46 (4.43)	9.22 (9.27)	5.62 (5.61)	6.07 (6.01)
[Zn(flu)$_2$(Cl)(H$_2$O)]	White	13.8	52.55 (52.59)	3.73 (3.75)	4.37 (4.38)	10.20 (10.23)	5.50 (5.52)	5.93 (5.95)
[Cd(flu)$_2$(Cl)(H$_2$O)]	White	11.9	48.92 (48.98)	3.50 (3.50)	4.05 (4.08)	16.34 (16.39)	5.10 (5.18)	5.54 (5.54)
[Hg(flu)$_2$(Cl)(H$_2$O)]	Brown	8.9	43.40 (43.40)	3.08 (3.10)	3.60 (3.62)	25.87 (25.91)	5.09 (5.08)	4.91 (4.90)
[Cr(flu)$_2$(Cl)(H$_2$O)]	Dark green	11.4	53.48 (53.71)	3.80 (3.83)	4.46 (4.47)	8.34 (8.31)	5.70 (5.67)	6.08 (6.07)
[Mn(flu)$_2$(Cl)(H$_2$O)]	Puff	12.6	53.41 (53.46)	3.77 (3.82)	4.41 (4.46)	8.70 (8.73)	5.51 (5.64)	6.04 (6.04)

Table 2
Fundamental infrared bands (cm^{-1}) of flumequine and its metal complexes.

Compound	ν_{OH} (COOH, H_2O)	$\nu_{(C=O)}$ pyridone	ν (COO) asym	ν (COO) sym	$\Delta\nu_{(asym-sym)}$	ν (C-N)	ν C-O stretch	ν M-O
Flumequine	3383	1616	-	-	-	1444	1260	-
$[Cu(flu)_2(Cl)(H_2O)]$	3445	1651	1536	1341	195	1428	1253	495
$[Co(flu)_2(Cl)(H_2O)]$	3440	1650	1598	1392	206	1488	1260	490
$[Ni\ (flu)_2Cl(H_2O)]$	3417	1648	1588	1385	203	1437	1260	447
$[Zn(flu)_2(Cl)(H_2O)]$	3431	1643	1598	1385	213	1490	1259	490
$[Cd(flu)_2(Cl)(H_2O)]$	3452	1647	1588	1382	206	1437	1258	492
$[Hg(flu)_2(Cl)(H_2O)]$	3470	1644	1544	1328	196	1420	1238	484
$[Cr(flu)_2(Cl)(H_2O)]$	3400	1650	1537	1328	205	1456	1260	517
$[Mn(flu)_2(Cl)(H_2O)]$	3436	1648	1598	1390	208	1451	1260	490

carbonyl group and indicates its participation in coordination with the metal ions. In the present study, the observed increase in the C═O stretching frequency can be attributed to electron redistribution upon complexation. A similar trend has been previously reported for flumequine metal complexes, where the shift to higher wavenumbers was explained by an increase in bond order due to coordination-induced electronic effects [14]. In contrast, the characteristic C–N stretching band of flumequine, located at 1444 cm^{-1}, remains essentially unchanged following complex formation, suggesting that the C–N group does not contribute to metal binding. The infrared spectrum of the free ligand displays a strong band at 1721 cm^{-1}, corresponding to the carbonyl stretching vibration of the carboxylic group. In the spectra of the metal complexes, this band does not appear in similar regions and replaced by two new absorptions appearing in the ranges of 1536–1598 cm^{-1} and 1328–1392 cm^{-1}, which are assigned to the asymmetric and symmetric stretching vibrations of the coordinated carboxylate group, respectively. The observed separation between the asymmetric and symmetric stretching frequencies ($\Delta\nu$) is small between (195–213 cm^{-1}) is characteristic of monodentate coordination of the carboxylate group to the metal center [34,35]. The carbonyl disappearance of the carboxylic group along with the appearance of asymmetric and symmetric stretching vibrations of the carboxylate group in the metal complexes, suggest the deprotonation and coordination of the ligand through the carboxylate group. This behavior is consistent with previously reported fluoroquinolone–metal complexes [14,36]. The remaining carboxylate vibration bands, ν(COO), ρ(COO), and ω(COO), which appeared at 773, 631, and 552 cm^{-1} in the free ligand, respectively, were shifted to different wavenumbers upon coordination. Furthermore, the C–O stretching vibration of free flumequine, originally observed at 1260 cm^{-1}, is retained in the spectra of the metal complexes with slight shifts within the range of 1253–1260 cm^{-1}, reflecting subtle changes in bonding upon coordination. Additional evidence for metal–ligand interaction is obtained from the far-infrared region, where new bands appearing between 447 and 517 cm^{-1} are attributed to metal–oxygen (M–O) stretching vibrations. These bands provide conclusive confirmation of coordination through oxygen donor atoms in the synthesized complexes. In general, flumequine is suggested to be coordinated with metal ions in a bidentate manner through the carbonyl oxygen of the pyridone ring and one oxygen atom of the carboxylate group. This coordination mode is consistent with previously published fluoroquinolone–metal complexes [37,38].

3.3. Electronic spectrum and magnetic moment measurements

The electronic absorption spectra of the metal complexes were recorded in the range 200–800 nm as shown in Fig S2. The observed spectral features, in combination with the measured magnetic susceptibility values, Table 3 suggests presence of octahedral geometries for the synthesized complexes. The magnetic moment values fell within the expected ranges for the corresponding metal ions, suggesting the absence of significant magnetic coupling effects. The Co(II) complex, $[Co(flu)_2(Cl)(H_2O)]$, displayed characteristic bands at 295, 310, and 330 nm, along with a broad visible band assigned to the $^4T_{1\,g}(F) \rightarrow {}^4T_{2\,g}(P)$ transition. The magnetic moment value of the cobalt complex (μ_eff = 6.06 B.M.) is indicative of a high-spin Co(II) (d^7) electronic configuration. The markedly enhanced magnetic moment relative to the spin-only value reflects a significant orbital contribution and pronounced spin–orbit coupling, which are characteristic features of cobalt (II) complexes

Table 3
Nujol mull electronic absorption spectra λ_{max} (nm), room temperature effective magnetic moment values (μ_{eff} 298°K) and geometries of flumequine metal complexes.

Complex	λ_{max} (nm)	μ_{eff}	Geometry
$[Cu(flu)_2(Cl)(H_2O)]$	295, 310 , 390	2.81	O_h
$[Co(flu)_2(Cl)(H_2O)]$	295, 310, 330	6.06	O_h
$[Ni\ (flu)_2Cl(H_2O)]$	295, 325, 415	4.71	O_h
$[Zn(flu)_2(Cl)(H_2O)]$	295, 320, 340	Diamagnetic	O_h
$[Cd(flu)_2(Cl)(H_2O)]$	280, 295, 315	Diamagnetic	O_h
$[Hg(flu)_2(Cl)(H_2O)]$	290, 320, 510	Diamagnetic	Oh
$[Cr(flu)_2(Cl)(H_2O)]$	295, 315, 330	6.9	Oh
$[Mn(flu)_2(Cl)(H_2O)]$	295, 470, 510	5.7	Oh

Such magnetic behavior may be closer to octahedral coordination environment around the cobalt center [39]. The Ni(II) complex showed absorption bands at 295, 325, and 415 nm corresponding to the $A_{2g}(F) \rightarrow {}^3T_{1g}(F)$

$A_{2g}(F) \rightarrow {}^3T_{1g}(P)$ transitions. The nickel complex exhibits a magnetic moment of 4.71 B.M., which is significantly higher than the spin-only value expected for a d^8 system. This enhanced magnetic behavior is consistent with a high-spin Ni(II) electronic configuration and suggests the presence of appreciable orbital contribution. Such a magnetic response suggests the assignment of octahedral coordination geometry around the nickel center. The Cu(II) complex exhibited bands at 295, 310, and 390 nm, where the broad visible band is attributed to the $^2E_g \rightarrow {}^2T_{2\,g}$ (D) transition. The copper complex shows a magnetic moment of 2.81 B.M., which exceeds the spin-only value expected for a Cu(II) (d^9) system with one unpaired electron. This enhanced magnetic moment can be attributed to strong spin–orbit coupling and Jahn–Teller distortion, both of which are characteristic of copper (II) complexes. Such magnetic behavior suggest that a distorted octahedral coordination geometry around the copper center [40,41]. The Cr(III) complex displayed absorption bands at 295, 315, and 330 nm assignable to the $^4A_{2\,g} \rightarrow {}^4T_{2\,g}$ (F), $^4A_{2\,g} \rightarrow {}^4T_{1\,g}(F)$ and $^4A_{2\,g} \rightarrow {}^4T_{1\,g}(p)$ transitions, respectively. The chromium complex exhibits a magnetic moment of 6.9 B.M., indicating a high-spin electronic configuration with a substantial number of unpaired electrons. The pronounced deviation from the spin-only values suggests a significant orbital contribution and possible spin–orbit coupling effects. Such magnetic behavior is consistent with an octahedral coordination environment around the chromium center, likely accompanied by a degree of structural distortion [42,43]. Similarly, the Mn(II) complex exhibited bands at 295, 470, and 510 nm due to$^4A_2g \rightarrow {}^4T_{2\,g}$ (F), $^4A_{2\,g} \rightarrow {}^4T_{1\,g}(F)$ and $^4A_{2\,g} \rightarrow {}^4T_{1\,g}(p)$ transitions. The

manganese complex exhibits a magnetic moment of 5.06 B.M., which is consistent with a high-spin Mn(II) (d^5) electronic configuration containing five unpaired electrons. The slightly reduced value relative to the theoretical spin-only moment can be attributed to covalency effects and experimental conditions. This magnetic behavior suggests the assignment of octahedral coordination geometry around the manganese center [42,43]. In contrast, the Zn(II), Cd(II), and Hg(II) complexes showed only ligand-to-metal charge transfer bands in the ultraviolet region due to their $d^{1\,0}$ electronic configurations, and no d–d transitions were observed. Therefore, the geometry could not be directly suggested from electronic spectra. The proposed geometry for these complexes is based on indirect evidence and by similarity with the corresponding transition metal complexes, taking into account similar stoichiometry and spectroscopic behavior [44]. The electronic spectra of the investigated complexes exhibit broad and overlapping bands, which makes the accurate determination of ligand field parameters difficult. Therefore, reliable calculation of ligand field parameters was not feasible in all cases. The structural features and coordination behavior of the complexes were discussed based on UV–Vis, IR, magnetic measurements, and molar conductivity data. Although single-crystal XRD was not available, this approach has been commonly used in similar studies on metal complexes with different types of ligands [45–48]. In such cases, researchers often rely on combined spectroscopic and magnetic data to suggest the most probable geometry. Therefore, the proposed geometries in this work are considered as probable rather than definite, taking into account the absence of crystallographic confirmation.

3.4. Electron spin resonance

The room-temperature ESR spectrum of the $[Cu(flu)_2(Cl)(H_2O)]$ complex displays an isotropic symmetric X-band signal characteristic of a polycrystalline sample, Fig. 2. The spectrum is defined by an effective g-value of approximately 2.11, along with a hyperfine coupling constant (A) of 135×10^{-4} cm^{-1}. The g value, being greater than the free electron value (2.0023), confirms the presence of Cu(II). The isotropic nature of the signal suggests dynamic averaging under the experimental conditions, limiting detailed geometric interpretation from ESR alone. The A value lies within the typical range reported for Cu(II) complexes, suggesting the assigned coordination environment

3.5. Computer analysis programs

The bond length, bond angles and dihedral angles of flumequine was measured by using Avogadro program, Table S1, S2 and S3. Charge density of flumequine atoms is calculated by applying hyper chem. program, Fig. 3 suggests flumequine coordination through oxygen of carbonyl group and oxygen of carboxylate group.

3.6. Thermal analysis studies (TG, DTA, DSC)

The thermal stability of the free ligand and its metal complexes was investigated using thermogravimetric techniques over a temperature range from 0 to 800 °C at a constant heating rate of 20 °C min^{-1} [49–51]. The obtained TGA curves exhibited well-defined multistep decomposition patterns, reflecting the sequential elimination of lattice and coordinated species followed by gradual degradation of the organic framework [52–54]. The corresponding temperature ranges, mass loss percentages, decomposition steps, and final residues assigned to metal oxide and organic residues products [55,56]—are summarized in Table 4. Differential thermal analysis (DTA) was employed to investigate the thermal behavior and stability of the synthesized compounds. Differential scanning calorimetry (DSC) differs from differential thermal analysis (DTA) in that both the sample and the reference are maintained at an identical, program-controlled temperature throughout the experiment, even when thermal events occur. DSC is widely applied to examine thermal transitions such as glass transition, melting, and crystallization processes. The DSC thermograms obtained distinct thermal features related to structural rearrangements, melting characteristics, and thermal decomposition, thereby offering complementary insights alongside thermogravimetric analysis [57–59].

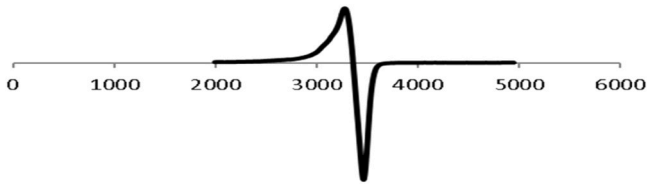

Fig. 2. ESR of Cu flumequine complex.

The differential thermal analysis (DTA) curve of the free flumequine ligand, Fig. 4, Fig. 6 and Table 5 exhibited three well-defined thermal exothermic peaks occurring at 94.66, 175.76, and 474.48 °C. Kinetic evaluation of these thermal processes yielded activation energy values closely between (16–565 kJ mol^{-1}), respectively. The calculated reaction order values are approximately found in the range of 0.8–1.3 indicate that the decomposition steps closely follow first-order reaction kinetics. These observations are consistent with the thermogravimetric analysis (TGA) results, which revealed three well-defined decomposition steps. The thermal decomposition of flumequine proceeds through three successive stages as revealed by TGA analysis, Table 4. The first stage (28.77–116.81the), corresponding to the elimination of small fragments such as CH_4, exhibits a reaction order of approximately ~1.3, indicating a process approaching first-order behavior. The second stage (116.81–230.87 °C), attributed to the loss of CO_2 and HF, shows a lower reaction order (~0.8), suggesting a more complex decomposition process. In the third stage (230.87–584.88 °C), corresponding to the breakdown of the organic backbone with the evolution of CO and C_2H_4, the reaction order is approximately ~1.0, indicating a process close to first-order behavior., as illustrated in Scheme 1.

The DTA thermogram of the $[Cr(flu)_2(Cl)(H_2O)]$ complex, Fig. 5, and Table 5 revealed three well-resolved exothermic thermal events occurring at 48.36, 233.33, and 392.84 °C. Kinetic analysis of these decomposition stages yielded activation energy values in the range of (51–56 kJ mol). The calculated reaction order values were found approximately between (1.1–2.5). The exothermic character of all thermal transitions further supports the proposed decomposition pathway. In addition, the TGA curve exhibited three distinct mass-loss steps, Table 4. The thermal decomposition of the chromium complex took place in three successive stages. In the first stage (30.73–165.23 °C), the complex lost two coordinated water molecules together with 2HCl, 4HF, and 4 CH_4. This stage showed a reaction order of approximately ~2.5, which indicates that the decomposition in this range is relatively complex. In the second stage (165.23–333.63 °C), the decomposition was mainly related to the loss of $4C_3H_5N$ fragments. The reaction order in this step was about ~1.5, suggesting that this stage is still more complex than an ideal first-order process. In the third stage (333.63–590.79 °C), further degradation occurred with the evolution of CO and $4CO_2$, together with the formation of Cr_2O_3 as the final residue with some organic remainder. The reaction order in this stage decreased to approximately ~1.2, indicating a process closer to first-order behavior compared with the earlier stages, as illustrated in Scheme 2.

In contrast, the thermal analysis of the $[Zn(flu)_2(Cl)(H_2O)]$ complex, as presented in Fig.S3 and Table 5, exhibited three well-defined exothermic peaks at 48.43 °C, 252.20 °C, and 475.06 °C, as determined from the DTA data. The corresponding activation energies for these events were closely to (20−51) kJ/mol. The reaction orders were in the range of 0.8–1.5 for the three peaks. The thermal decomposition of the Zn(II) complex proceeded in three successive stages, Table 4. In the first stage (38.38–192.13 °C), the complex undergo dehydration with the loss of coordinated water molecules along with small volatile fragments. This step showed a reaction order of approximately ~1.4,

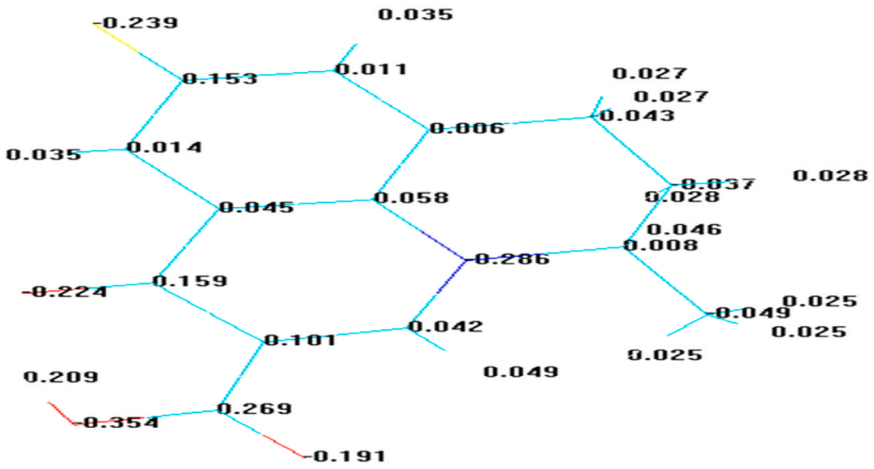

Fig. 3. Charge density of flumequine.

Table 4
Thermogravimetric analysis of flumequine and its selected metal complexes.

Complex	Temp. (°C) TGA	Wt. Loss %		Assignment
		Calc	Foud	
Flumequine	28.77–116.81°C	4.40	4.57	Elimination of CH_4
	116.81–230.87°C	34.61	35.56	Loss of CO_2 and HF
	230.87–584.88°C	35.56	35.65	Loss of CO and C_2H_4
$[Zn(flu)_2(Cl)(H_2O)]$	38.38–192.13°C	7.7	7.5	Dehydration of $H_2O$and losing of $2CH_4$
	192.13–314.26°C	22.7	22.83	Loss of 2HF, HCL
	162.5–589.7 °C	30.52	30.56	Decomposition of $2CO_2$, 2CO and formation of ZnO with organic residue
$[Cr(flu)_2(Cl)(H_2O)]$	30.73–165.23 °C	26.21	26.01	Dehydration of 2 H_2O and loss of 2HCL, 4HF and $4CH_4$
	165.23–333.63 °C	31.49	32.57	Loss of 4 C_3H_5N
	333.63–590.79 °C	24.78	24.95	Degradation of CO, $4CO_2$ and formation of Cr_2O_3 with organic residue
$[Ni\ (flu)_2Cl(H_2O)]$	24.27–137.25 °C	21.25	21.04	Dehydration of H_2O and elimination of HCl and 2HF
	137.25–581.65 °C	61.31	61.35	Decomposition of the last part of ligand and formation of NiO with organic part

indicating a process close to first-order behavior with slight deviation. In the second stage (192.13–314.26 °C), further decomposition occurred with the release of HF and HCl, accompanied by the breakdown of part of the ligand structure. The reaction order in this stage was about ~0.8, suggesting a simpler process, close to first-order kinetics. In the final stage (314.26–589.70 °C), complete degradation of the organic ligand took place with the evolution of CO_2 and CO, leading to the formation of ZnO as the final residue. This stage exhibited a reaction order of approximately ~1.5, indicating a relatively more complex decomposition step compared to the previous stage. The exothermic character of these thermal transitions is further confirmed by Scheme S1. The DTA profile of the $[Ni(flu)_2Cl(H_2O)]$ complex, as presented in Fig.S4 and Table 5, exhibited three distinct exothermic peaks at 81.83 °C, 310.01 °C, and 360.33 °C. The corresponding activation energies for these thermal events ranged between (19–180 kJ/mol). The reaction orders were closely between 1 and 1.8. The thermal decomposition of the Ni(II) complex occurred in two main stages, Table 4. In the first stage (24.27–137.25 °C), the complex lost the coordinated water molecules along with the release of HCl and HF. The reaction order in this stage was found to be around ~1.0–1.3, indicating that the process follows nearly first-order behavior. In the second stage (137.25–581.65 °C), further decomposition of the remaining ligand took place, leading to the formation of NiO as the final residue with some organic remnants. The reaction order values in this stage ranged from ~1.3 to ~1.8, suggesting a more complex decomposition step compared to the first stage. The presence of more than one reaction order value within the same stage can be attributed to overlapping processes or the gradual breakdown of different parts of the ligand during heating. The exothermic nature of all three transitions is further illustrated in Scheme S2.

The relationship between ln ΔT and 10^{3} /T exhibited good linearity for all the studied complexes, which supports the reliable estimation of activation energy values using least-squares analysis, Fig. S5–S7. The calculated thermodynamic parameters are listed in Table 6. Moreover, the reaction order (n) was determined by using the peak symmetry method based on the shape of the DTA peaks which is commonly applied for kinetic analysis of solid-state thermal decomposition processes [60]. The obtained values are approximate and may vary slightly due to overlapping processes during the thermal decomposition.

The DSC thermograms of flumequine and its selected metal complexes, Fig.S.(8–11) Table 6 display several characteristic thermal transitions associated with glass transition, crystallization, and melting phenomena. $[Ni\ (flu)_2Cl(H_2O)]$ complex exhibited the highest Tg values, recorded at 174.79°. In contrast, the Tg values of flumequine and remaining complexes were significantly lower, ranging between 133.23 and 158.17 °C. The crystallization temperature (Tc) of $[Ni\ (flu)_2Cl(H_2O)]$ was 361.33 °C, indicating that the systems acquired sufficient energy to form highly ordered crystalline arrangements, followed by the release of heat through an exothermic transition. Among all complexes, $[Ni(Cef)Cl(H_2O)_3]$ exhibited the highest Tc, whereas flumequine and other complexes showed lower Tc values in the range of 228.87–254.7 °C Furthermore, all prepared complexes demonstrated melting points above 300 °C. The DSC plots allowed precise determination of the melting temperatures through the observed melting transitions, during which the complexes absorbed heat until complete melting of the crystalline phase was achieved.

3.7. Morphology

3.7.1. Powder X-ray diffraction (XRD)

Powder x-ray diffraction (XRD) analysis was employed to investigate the crystalline nature and phase composition of the synthesized compounds. This technique provides essential information about crystalline nature and structural order through the analysis of diffraction patterns. Powder X-ray diffraction measurements were performed to investigate the solid-state structures of the Hg– and Zn–flumequine complexes, the data were indexed and refined using GSAS software and Rietveld

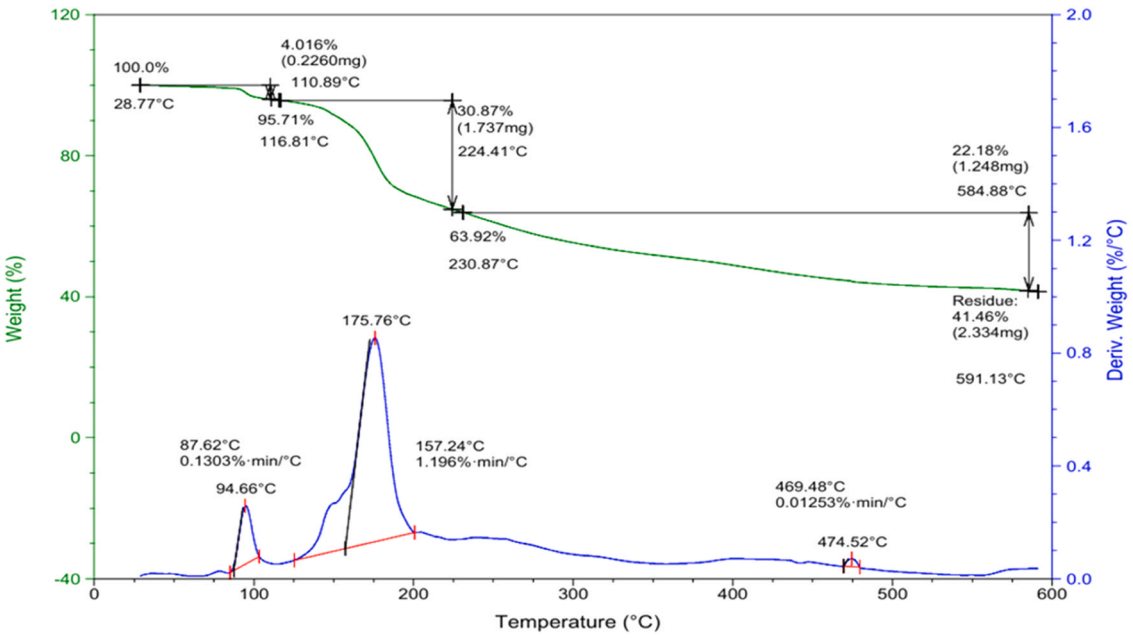

Fig. 4. TGA and DTA of flumequine ligand.

Table 5
Kinetic parameters of thermal decomposition of flumequine and its selected metal complexes.

Complex	Type	Tm (°K)	E_a kJ mol^{-1}	N	α_m	$\Delta S^{\#}$ kJ K^{-1} mol^{-1}	$\Delta H^{\#}$ kJ mol^{-1}	Z S^{-1}
Flumequine	Exo	94.66	90.34	1.26	0.59	-0.27	-25.80	0.11
	Exo	175.76	16.37	0.84	0.66	-0.30	-52.20	0.011
	Exo	474.48	565.352	1.03	0.63	-0.28	-134.79	0.14
$[Zn(flu)_2(Cl)(H_2O)]$	Exo	48.43	50.715	1.41	0.67	-0.27	-12.89	0.13
	Exo	252.2	20.369	0.84	0.66	-0.30	-75.96	0.01
	Exo	475.06	48.221	1.48	0.56	-0.30	-144.69	0.012
$[Cr(flu)_2(Cl)(H_2O)]$	Exo	48.36	51.55	2.47	0.46	-0.27	-12.87	0.13
	Exo	233.33	55.42	1.54	0.55	-0.29	-63.04	0.03
	Exo	392.84	53.68	1.16	0.60	-0.30	-118.06	0.016
$[Ni\ (flu)_2Cl(H_2O)]$	Exo	81.83	19.51	1.35	0.58	-0.28	-23.145	0.03
	Exo	310.01	180.13	1.03	0.63	-0.29	-88.82	0.069
	Exo	360.33	53.58	1.75	0.53	-0.30	-107.77	0.017

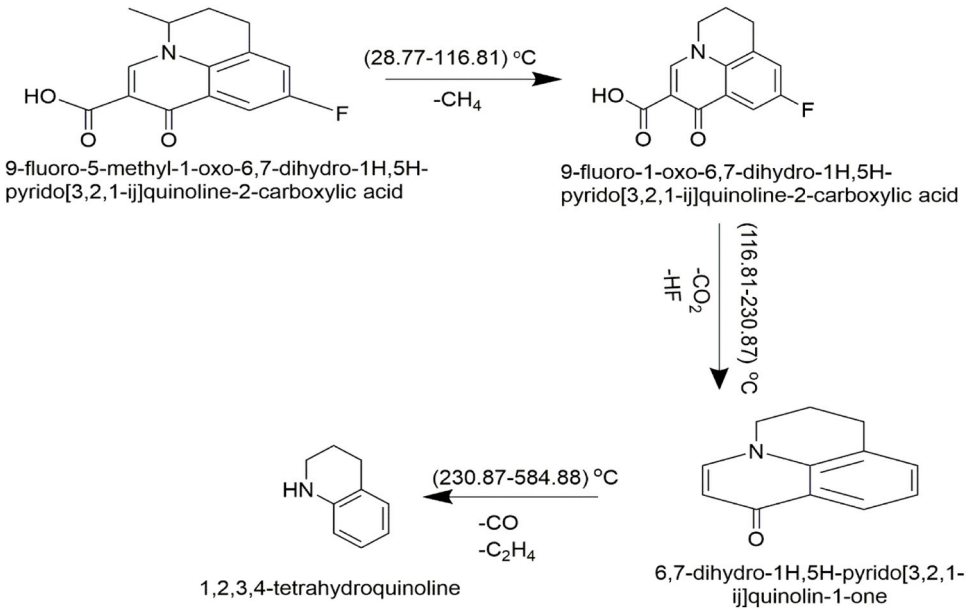

Scheme 1. Thermolysis of flumequine ligand.

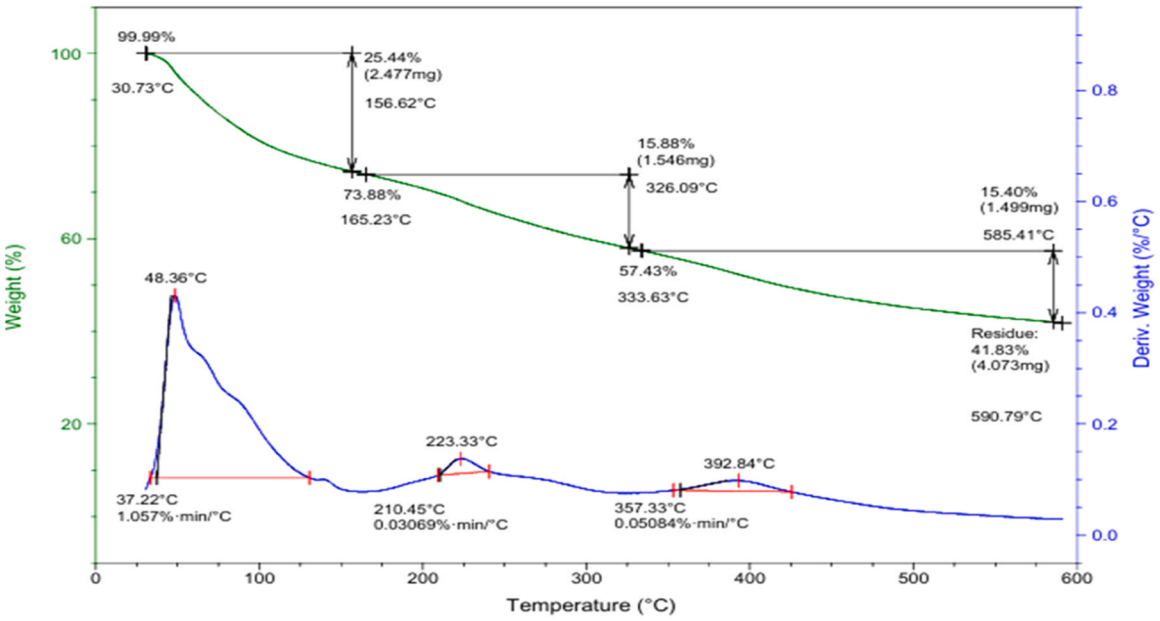

Fig. 5. TGA and DTA of chromium flumequine complex.

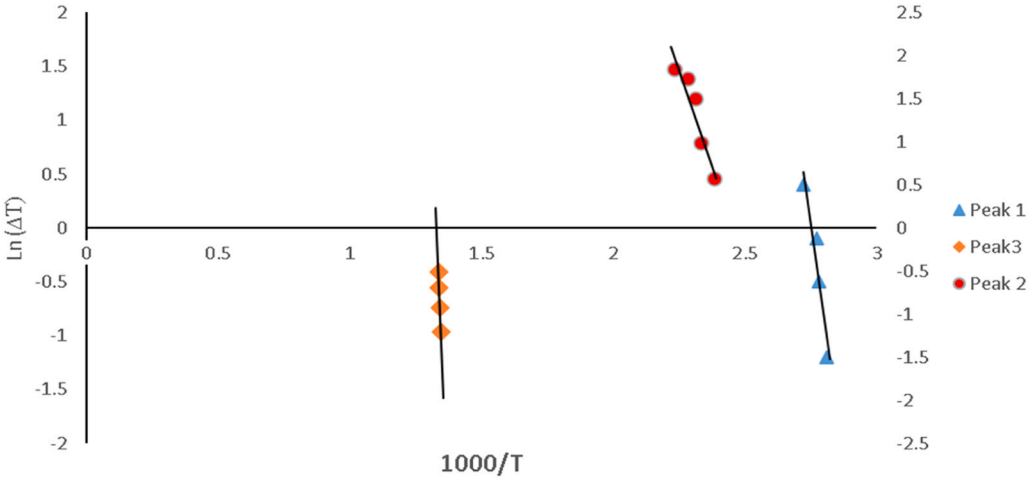

Fig. 6. lnΔT against 10^3/T relations for flumequine.

refinement was performed. The XRD pattern of the Hg–flumequine complex, recorded over a 2θ range of 0–80°, displayed several sharp and intense diffraction peaks, indicating a well-developed crystalline structure. Prominent reflections observed on approximately21.19, 27.88, 30.96, 32.61, 40.01, 43.59, 45.97 suggest the presence of a highly ordered lattice. Indexing of the diffraction data revealed unit cell parameters of a = 7.127 Å, b = 7.854 Å, and c = 4.899 Å, with a monoclinic crystal system (β = 115.44°, V = 247.68 Å^3). These structural features are consistent with monoclinic coordination frameworks commonly reported for metal–antibiotic complexes. The average crystallite size estimated using the Debye–Scherrer equation.

$$D = K\lambda / (\beta \cos\theta) \quad (1)$$

Where D is the crystallite size, K is the shape factor, λ is the X-ray wavelength, β is the full width at half maximum (FWHM) of the diffraction peak, and θ is the Bragg angle.

The crystalline size was found to be 12.65 ± 1.15 nm, suggesting the nanocrystalline nature of the Hg–flumequine complex. the theoretical density (ρ) of the complex was evaluated using the relation: ($\rho = \frac{ZM}{N_A V}$) where Z is the number of formula units per unit cell (Z = 1), M is the molecular weight of the complex (774.1 g mol^{-1}), N_a is Avogadro's number, and V is the unit cell volume in cm^{-3}. the theoretical density was found to be 5.02 g cm^{-3} . Furthermore, the calculated number of unit cells per crystallite (n ≈ 8.1 × 10 ^{3}) indicates that each nanoparticle consists of several thousand well-ordered unit cells, Table 7 and Fig. 7. In contrast, the XRD pattern of the Zn–flumequine complex exhibited broad and low-intensity diffraction features within the 2θ range of 10–50°, suggesting a nanocrystalline to partially amorphous structure. A broad diffraction band centered around 12–40° confirms the formation of a new coordination phase distinct from the free ligand. The refined lattice parameters (a = 3.92 Å, b = 6.69 Å, c = 15.42 Å, β = 117.16°) correspond to a monoclinic unit cell with a calculated volume of 359.99 Å^3 . The average crystallite size was estimated to be 10.85 ± 1.18 nm, further suggesting the nanocrystalline character of the Zn–flumequine complex. The theoretical density was calculated to be approximately 2.9 g cm^{-3} (Z = 1, M=638.5 gm/mol), and the number of unit cells per crystallite was estimated at n ≈ 3.5 × 10^3, Table 8 and Fig. 8. The refinement quality varied among the complexes, where the

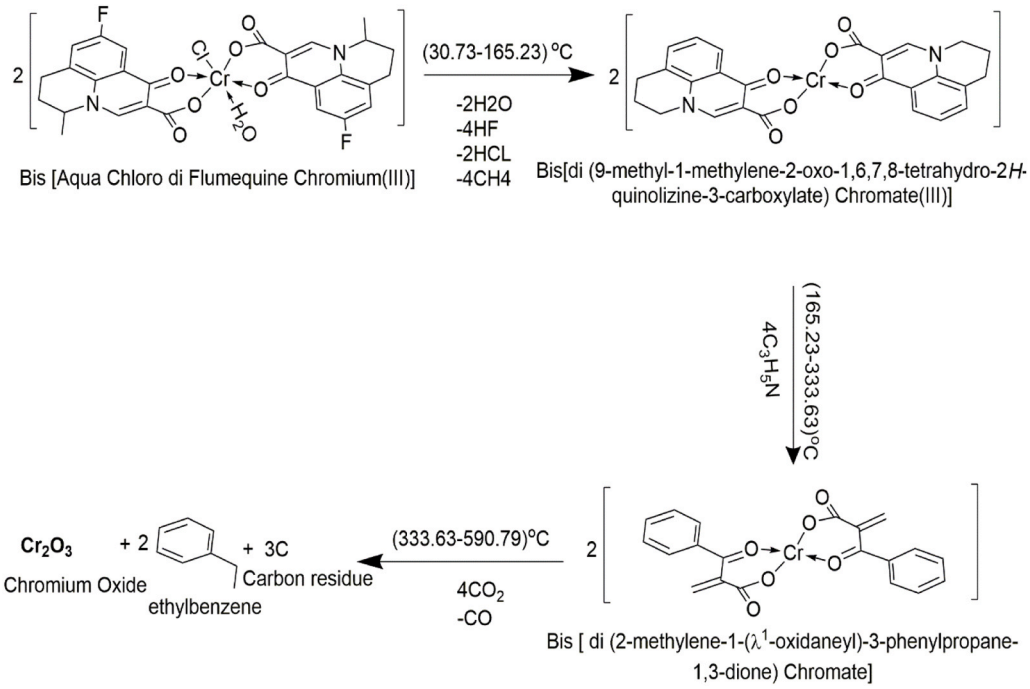

Scheme 2. Thermolysis of chromium flumequine complex.

Table 6
Thermal transitions of flumequine and selected complexes.

Compound	Thermal transitions (°C)	
	T_g	T_c
Flumequine	149.86	241.69
$[Zn(flu)_2(Cl)(H_2O)]$	133.23	254.7
$[Cr(flu)_2(Cl)(H_2O)]$	158.17	228.87
$[Ni\ (flu)_2Cl(H_2O)]$	174.79	361.33

Table 7
X-Ray differaction data of Hg-flumequine complex.

Observed2θ	Calculated2θ	h	k	l	d spacing	FWHM	Diff 2θ
21.19	21.14	0	3	1	4.19	0.483	0.05
27.88	27.88	2	2	2	3.19	0.352	0.00
30.96	30.93	2	3	1	2.88	0.911	0.03
32.61	32.65	1	1	6	2.73	0.774	-0.04
40.01	39.93	0	4	6	2.25	0.727	0.08
43.59	43.52	2	5	3	2.07	0.557	0.07
45.97	45.89	2	3	7	1.97	0.823	0.08

Zn(II) complex showed good agreement ($R \approx 9.23$, $\chi^2 \approx 2.13$), while the Hg(II) complex exhibited reasonable agreement ($R \approx 12.79$, $\chi^2 \approx 3.45$). These findings indicate that the Zn–flumequine complex consists of nanoscale crystallites with compact packing and structural order, despite its reduced crystallinity compared to the Hg analogue.

3.7.2. Scanning electron microscopy (SEM)

SEM analysis of flumequine metal complexes revealed metal-

Table 8
X-Ray differaction data of Zn-flumequine complex.

Observed2θ	Calculated2θ	h	k	l	d spacing	FWHM	Diff 2θ
12.14	12.06	0	1	0	7.32	0.712	0.08
15.45	15.49	3	1	0	5.71	0.537	-0.04
20.02	19.99	3	0	2	4.48	0.761	0.03
24.85	24.77	1	2	0	3.60	0.464	0.08
26.70	26.77	-6	1	2	3.32	0.626	-0.07
29.84	29.90	1	0	-3	2.98	1.01	-0.06
33.71	33.75	0	2	0	2.65	1.09	-0.04
35.99	36.01	1	1	0	2.48	0.809	-0.02
38.45	38.45	1	0	- 5	2.33	1.24	0.00

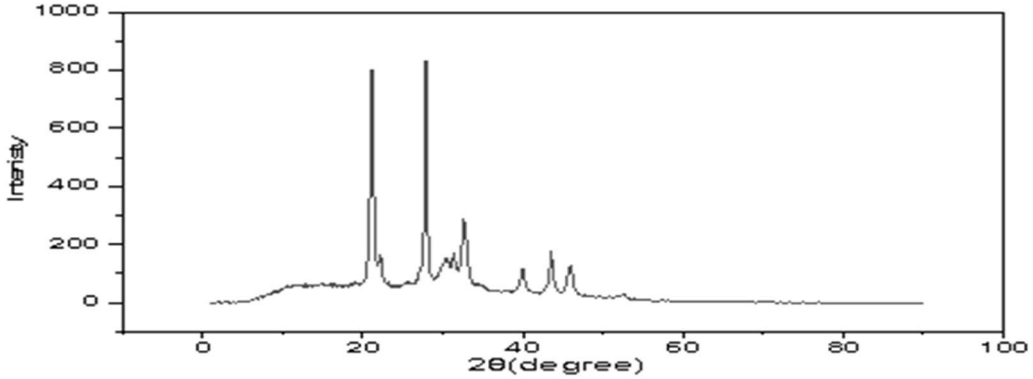

Fig. 7. XRD of Hg flumequine complex.

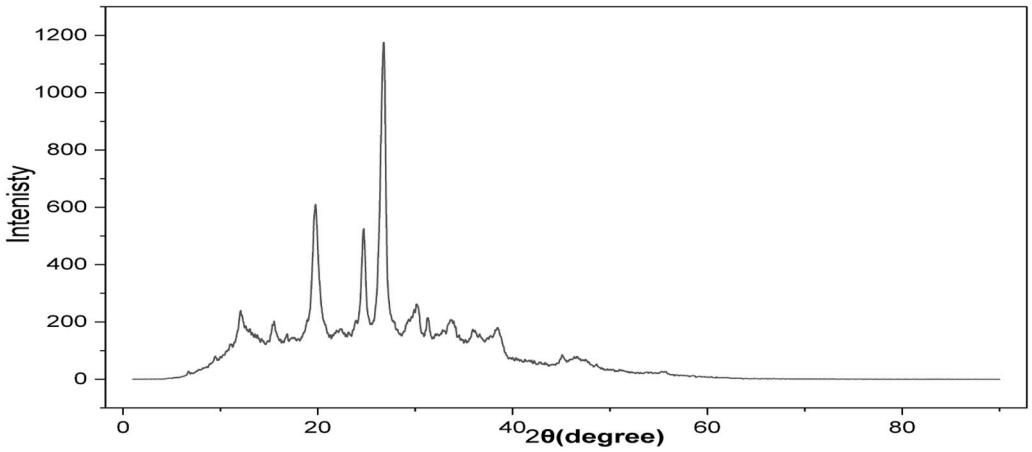

Fig. 8. XRD of Zn flumequine complex.

dependent variations in surface morphology [61]. The Cd–flumequine complex exhibited a dense and compact surface composed of fused, irregular particles with low porosity, Fig. 9(a). In contrast, the Cr–flumequine complex showed an aggregated morphology with irregular particles, moderate porosity, and visible surface cracks, indicating partial compaction Fig. 9(b). The Mn–flumequine complex displayed a highly porous, sponge-like structure formed by loosely packed fine particles, reflecting an open and semi-amorphous architecture, Fig. 9(c). These observations confirm that metal coordination significantly influences the microstructural features of flumequine complexes.

3.8. Structural interpretation

Based on the combined analytical and spectroscopic results, the structural features of the synthesized flumequine metal complexes were predicted, and the proposed coordination models are presented in Fig. 10. Elemental analysis data were in good agreement with the suggested molecular compositions, suggesting the stoichiometry of the complexes. Infrared spectral analysis provided clear evidence for the involvement of specific functional groups of flumequine in metal coordination. Furthermore, the molar conductivity of the synthesized complexes was measured, and the obtained low values indicate their non-electrolytic nature. This behavior suggests that the chloride ions are coordinated rather than existing as free ions in solution. Furthermore, thermal analysis supports the presence of coordinated water molecules within the complex structure, based on the obtained data the suggested structure for all complexes is $[M(flu)_2ClH_2O]$.

3.9. Biological activity

Antimicrobial activity was evaluated using an in vitro method. For each compound, a single inhibition zone value was obtained and used for comparative assessment of the antibacterial and antifungal activity. Therefore, the results are presented to indicate general trends in activity rather than detailed statistical significance The antimicrobial performance of flumequine and its Cu(II), Co(II), Zn(II), and Mn(II) complexes was examined against Gram-positive bacteria (*Staphylococcus aureus* ATCC 6538 P and *Bacillus subtilis* ATCC 19659), Gram-negative bacteria

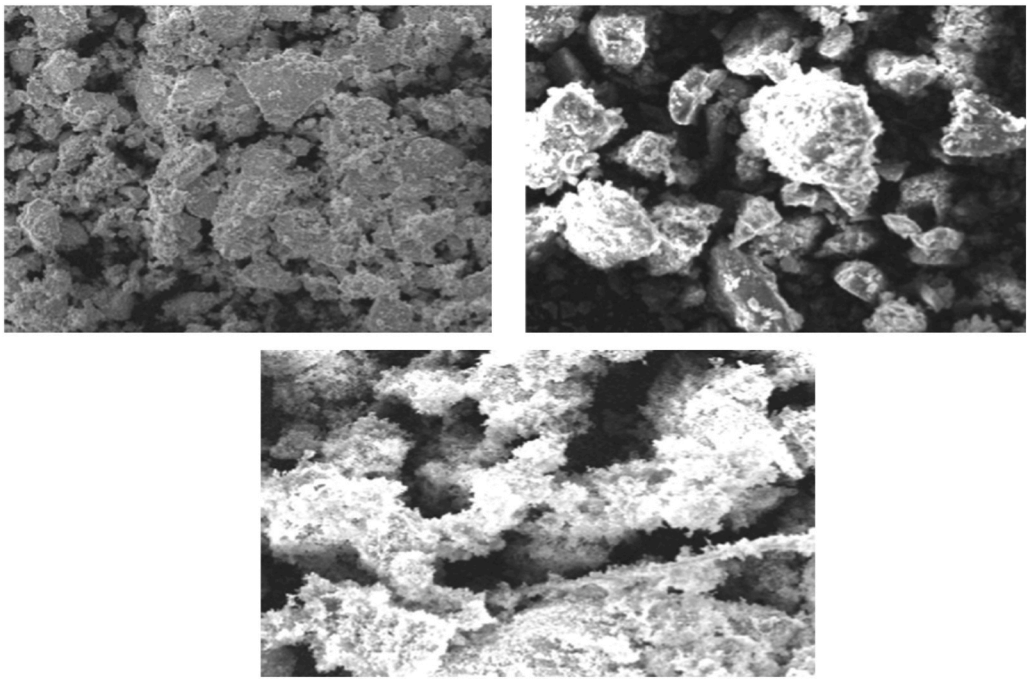

Fig. 9. SEM image of Cd flumequine complex(a), Cr flumequine complex(b) and Mn flumequine complex (c).

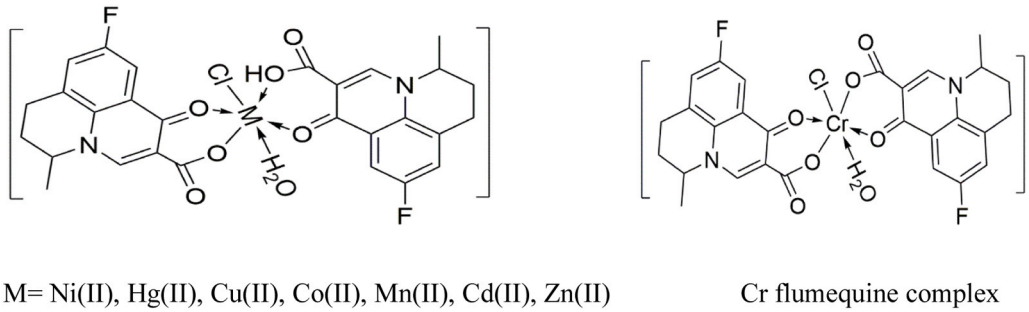

Fig. 10. Proposed structure of flumequine complexes.

(*Escherichia coli* ATCC 8739 and *Pseudomonas aeruginosa* ATCC 9027), and the fungal strain *Candida albicans* ATCC 2091 using ciprofloxacin and clotrimazole as references, Table 9 Fig.S12. Against *S. aureus*, the free ligand exhibited a inhibition zone (29 mm), but for Cu(II), Zn(II), Mn(II) and Co(II) complexes showed inhibition zone (30, 27, 15 and 26 mm) respectively, For *B. subtilis*, flumequine, Cu(II), Co(II), Zn(II), and Mn(II) complexes showed inhibition zone (28, 29, 27, 27, 25 mm) respectively. For Gram-negative strains, flumequine showed activity against *E. coli* (30 mm), Cu(II), Co(II), Zn(II) and Mn(II) complexes give inhibition zone equal (31, 31, 30, 29 mm). Comparable inhibition patterns were recorded against *P. aeruginosa*, for flumequine and its Cu(II), Co(II), Zn(II) and Mn(II) metal complexes give values at (28, 27, 26, 27 and 27 mm). In the case of *Candida albicans* fungi, flumequine exhibited an inhibition zone of mm, for the Cu(II), Co(II), Zn(II), and Mn(II) complexes (29, 28, 27 and 26 mm). Overall, the antibacterial activity results showed that the metal complexes exhibited either lower or comparable activity to the free flumequine ligand against the tested bacterial strains, between the investigated complexes, the Cu(II) and Zn (II) complexes showed the highest activity, while the Mn(II) complex exhibited relatively lower activity. In comparison with the reference drug (ciprofloxacin), the activity of the synthesized complexes was found to be comparable in many cases, particularly against E. coli and P. aeruginosa, although slightly lower in some instances. The antifungal activity results showed that the tested compounds exhibited higher inhibition zone values than the reference drug (clotrimazole) against Candida albicans. These findings suggest that coordination of flumequine with metal ions does not necessarily enhance the antimicrobial activity but may influence it depending on the nature of the metal ion and the tested microorganism. The observed Change in activity for several metal complexes relative to the free ligand can be rationalized based on chelation theory and the overtone concept [62,63], where coordination reduces ligand polarity and facilitates diffusion through microbial cell membranes [64]. The results obtained should be considered preliminary, as the measurements were carried out as an initial screening step. Similar approaches have been reported in previous studies [65,66], where in vitro antimicrobial activity is presented for general evaluation of the compounds.

3.10. Molecular docking

Flumequine is an antibacterial agent that shows activity against both Gram-positive and Gram-negative bacteria. It belongs to the fluoroquinolone group, which is known to act by interfering with bacterial DNA replication through targeting enzymes such as DNA gyrase and topoisomerase IV.Based on this mode of action, DNA gyrase was selected in this study as a representative bacterial target to evaluate the binding behavior of flumequine and its corresponding metal complexes. DNA gyrase is a bacterial enzyme that belongs to the type II topoisomerase family and plays an essential role in DNA replication. It consists of four subunits, two GyrA and two GyrB (A_2B_2), which work together in a coordinated way. The GyrA subunits are mainly responsible for binding and cleaving DNA, while the GyrB subunits contain the ATP-binding sites that provide the energy needed for the enzyme activity. In terms of structure, DNA gyrase has a flexible, clamp-like shape that can open and close around the DNA molecule. It is composed of different regions, including an ATPase domain, a central part responsible for DNA interaction and cleavage, and a C-terminal region that helps in stabilizing the DNA. The enzyme is not rigid and undergoes continuous structural changes during its function, which allows it to control DNA topology effectively. This structural organization is generally similar across different bacterial species, which highlights its importance and makes DNA gyrase a suitable model for studying this type of enzyme [67–69].

In this context, docking studies involving flumequine and its Cu(II), Co(II), and Zn (II) complexes were conducted to explore their potential interactions with DNA gyrase and to assess the influence of metal coordination on enzyme binding and possible anti-bacterial activity.

To validate the docking protocol, a redocking procedure was performed using the co-crystallized ligand, moxifloxacin, within the active site of DNA gyrase (PDB ID: 4Z2C). The docked pose was compared with the original crystallographic conformation, yielding a root-mean-square deviation (RMSD) value of 0.45 Å. This low RMSD value indicates a high level of agreement between the predicted and experimental binding modes, confirming the reliability of the docking protocol, Fig. 11.

Molecular docking of the free flumequine ligand within the active site of the DNA gyrase (PDB ID: 4Z2C) revealed a favorable binding affinity, with a calculated binding energy of −8.1 kcal mol^{-1} . Analysis

Table 9
Biological activity of flumequine and selected metal complexes.

Compounds	*S. aureus*		*B. subtilis*		*P. aeruginosa*		*E. coli*		*Candida*	
	DMSO (mm)	Compound (mm)	DMSO (mm)	Compound (mm)	DMSO (mm)	Compound (mm)	DMSO (mm)	Compound (mm)	DMSO (mm)	Compound (mm)
DMSO	15	15	15	16	15	16	15	15	15	15
Flumequine	15	29	15	28	15	28	15	30	15	29
Mn-flumequine complex	15	15	15	25	15	27	15	29	15	26
Co-flumequine complex	15	26	15	27	15	26	15	31	15	28
Zn-flumequine complex	15	27	15	27	15	27	15	30	15	27
Cu-flumequine complex	15	30	15	29	15	27	15	31	15	29
Ciprofloxacin	9	30	10	30	9	30	9	30	-	-
Clotrimazole	-	-	-	-	-	-	-	-	9	18

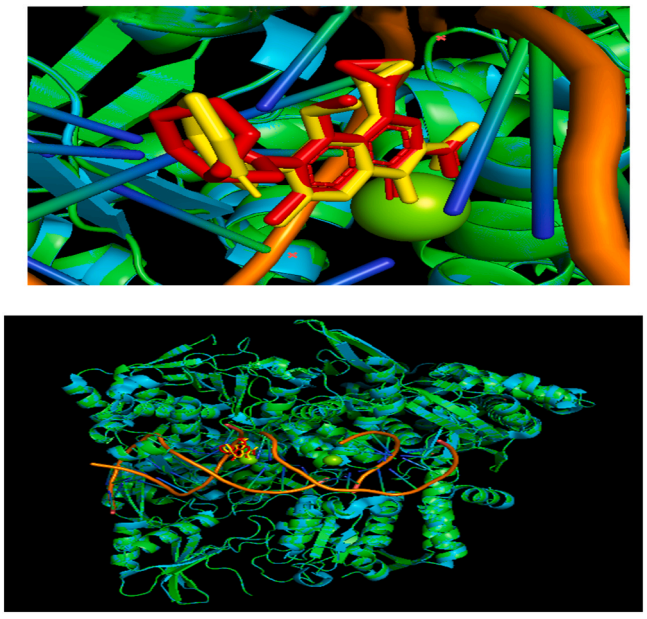

Fig. 11. Overly of the native and re-docked ligand (moxifloxacin) in the active site of 4Z2C.

of the predicted binding mode indicated that flumequine is stabilized within the enzyme pocket through multiple hydrogen-bonding interactions involving ASN B:326 and ASN B:179. In addition to these polar contacts, Vander Waals interaction was provided with DA H9, while a carbon hydrogen interaction with GLY B:328 further reinforced ligand–receptor binding. Also, carbon fluorine and fluorine interaction occurred with GLY B:171, hydrophobic interactions are presented by Alkyl, pi alkyl and pi-pi-T shaped interactions with ALA B:177. These interactions collectively contribute to the stable accommodation of flumequine within the active site, as depicted in Fig. 12 and summarized in Table S4.

Docking simulations of the Cu–flumequine complex within the active site of DNA gyrase (PDB ID:4Z2C) revealed a binding energy of -11.8 kcal mol^{-1} , indicating a highly favorable and stable interaction. Analysis of the binding mode showed the formation of a conventional hydrogen bond with the DNA base (DA F:10) and ARG D:633, contributing to stabilizing the complex within the binding pocket. the DNA base (DC F:8), in addition, halogen (fluorine) interactions were observed with ASP D:628, GLY D:627, and ARG D:633. Notably, hydrophobic interactions, including alkyl interaction were also observed with LYS D:464, and π–alkyl contacts with DNA base(DC F:8 and DA E:7) and pi-pi-T shaped with (DAE:7) contributing to additional stabilization of the ligand within the enzyme–DNA complex. These combined interactions account for the strong binding affinity of the Cu–flumequine complex. as illustrated in Fig. 13 and summarized in Table.S5

Docking simulations of the Co–flumequine complex within the active site of DNA gyrase (PDB ID:4Z2C) revealed a binding energy of -11.4 kcal mol^{-1} , indicating a favorable and stable interaction. Detailed analysis of the binding mode demonstrated the formation of a conventional hydrogen bond with the DNA base (DA F:9, DG E:9 and DC F:8), contributing to anchoring the complex within the binding pocket. In addition, multiple halogen (fluorine) interactions were observed with nucleotides DA F:9, DT E:10, and DT E:11, which further enhanced the binding affinity of the complex. Moreover, hydrophobic interactions were identified, including alkyl and π–alkyl contacts with amino acid residues LYS D:464 and LYS D:469, playing a significant role in stabilizing the ligand within the enzyme–DNA complex. The presence of carbon–hydrogen bonding interactions with (DC E:8) also contributed to additional stabilization of the system., as illustrated in Fig. 14 and summarized in Table.S6

Docking simulations of the Zn–flumequine complex within the active site of DNA gyrase revealed a binding energy of -13.0 kcal mol^{-1} , indicating a highly favorable and stable interaction. Analysis of the binding mode demonstrated the formation of conventional hydrogen bonds with DNA bases (DA F:9 and DA F:10) and SER D:466, contributing to anchoring the complex within the binding pocket. In addition, a halogen (fluorine) interaction was observed with the amino acid residue (SER D:466), further enhancing the binding affinity. Furthermore, a Pi–Pi T-shaped interaction was identified with the DNA base (DT E:10), supporting favorable stacking interactions. Additional hydrophobic interactions, including π–alkyl contacts, were observed with nucleotides DA F:7, DC F:8, DA E:7 and DT F:6. A carbon–hydrogen bond involving DC E:8 also contributed to the overall stabilization of the complex, as illustrated in Fig. 15 and summarized in Table.S7.

A comparative molecular docking analysis was performed to evaluate the binding behavior of flumequine and its metal complexes toward

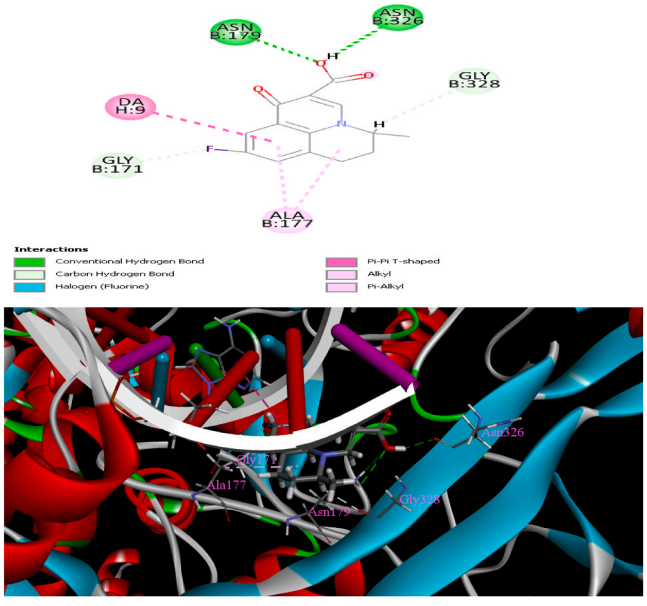

Fig. 12. Binding pose of flumequine and 4Z2C (2D), (3D) after docking.

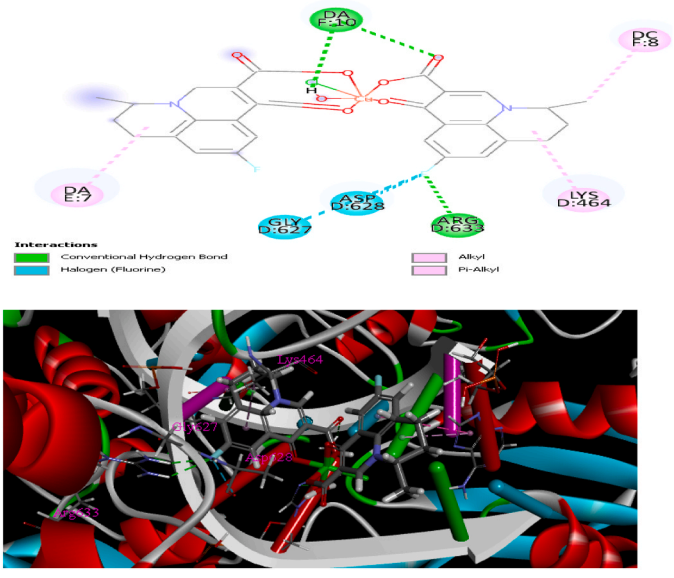

Fig. 13. Binding pose of Cu-flumequine complex and 4Z2C (2D), (3D) after docking.

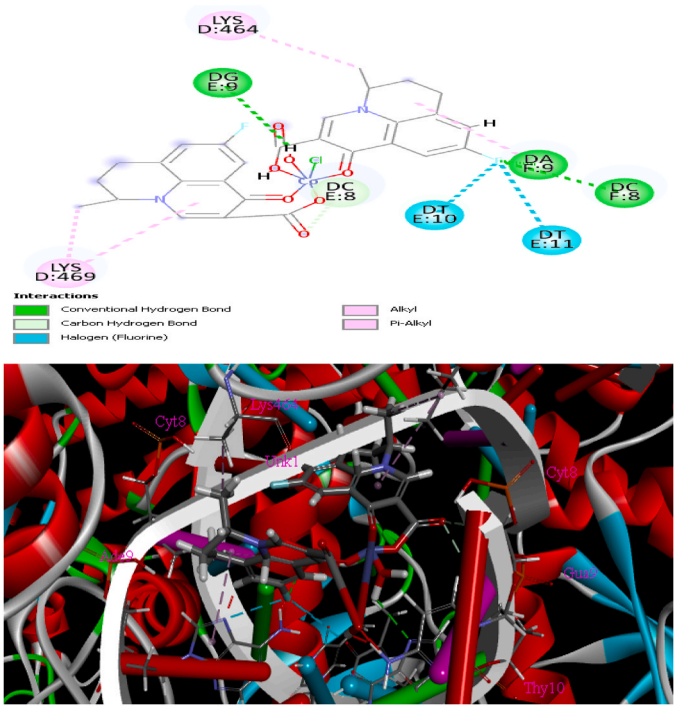

Fig. 14. Binding pose of Co flumequine complex with 4Z2C (2D), (3D) after docking.

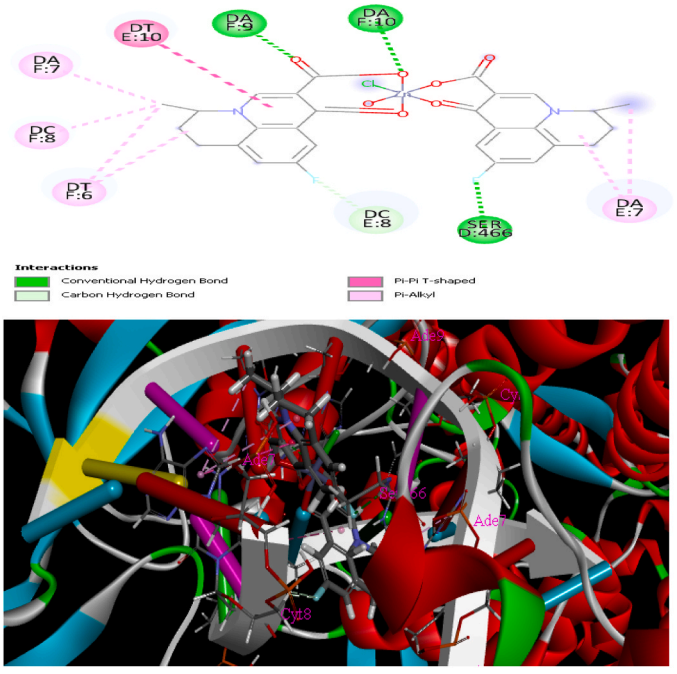

Fig. 15. Binding pose of Zn flumequine complex with4Z2C (2D), (3D) after docking.

DNA gyrase (PDB ID: 4Z2C). The calculated binding energies revealed a clear difference in affinity, where the Zn–flumequine complex exhibited the highest binding affinity (−13.0 kcal mol^{-1}), followed by the Cu– and Co–flumequine complexes (−11.8 and −11.4 kcal mol^{-1}, respectively), while the free flumequine ligand showed the lowest binding affinity (−8.8 kcal mol^{-1}). These results indicate that metal coordination enhances the interaction of flumequine within the active site of the target enzyme. A closer inspection of the binding modes showed that the superior binding affinity of the Zn(II) complex can be attributed to the formation of multiple stabilizing interactions within the active site. The Zn–flumequine complex formed several conventional hydrogen bonds with DNA bases (DA F:9 and DA F:10), in addition to a halogen (fluorine) interaction with SER D:466. Furthermore, π–π T-shaped interaction with DT E:10 and additional hydrophobic π–alkyl interactions with DA F:7, DC F:8, and DT F:6 contributed significantly to stabilizing the complex. Notably, the Zn complex interacted with a larger number of nucleotides compared to the other complexes, which explains its higher binding affinity. Similarly, the Cu(II) and Co(II) complexes exhibited stronger binding affinities than the free ligand due to the presence of multiple interactions with surrounding nucleotides and amino acid residues. These interactions included hydrogen bonding, halogen interactions, and hydrophobic contacts, which were more numerous and diverse than those observed for the free flumequine ligand. In contrast, the free ligand showed fewer interactions and a more limited binding network within the active site, resulting in its lower docking score.

Despite the enhanced binding affinities observed for the metal complexes, the biological activity results demonstrated that the free flumequine ligand exhibited higher antibacterial activity. This apparent discrepancy can be explained by considering that biological activity is not governed solely by binding affinity. Factors such as molecular size, lipophilicity, solubility, and the ability to penetrate bacterial cell membranes play a critical role in determining the overall antimicrobial effect. The free ligand, being smaller and less complex, may diffuse more efficiently through the bacterial membrane and reach its intracellular target more effectively than its metal complexes. Therefore, while the docking results suggest stronger molecular interactions for the metal complexes, these findings should be interpreted as supportive rather than definitive predictors of biological activity [70,71].

4. Conclusion

In this study, a series of transition metal complexes of flumequine were successfully synthesized and comprehensively characterized to elucidate the impact of metal coordination on their structural, physicochemical, and biological properties. Spectroscopic investigations suggested that the coordination mode of flumequine through oxygen donor atoms, while electronic spectral data and magnetic susceptibility measurements consistent with octahedral geometries for the transition metal complexes. Thermal analyses demonstrated multistep decomposition behavior and revealed enhanced thermal stability of the metal complexes compared to the free ligand. Solid-state studies using XRD and SEM showed metal-dependent variations in crystallinity and surface morphology, suggesting the formation of nanocrystalline coordination frameworks. The biological evaluation revealed variations in antimicrobial activity among the investigated complexes compared to the free ligand. Difference in inhibition zone diameters were observed among the synthesized complexes, indicating that the nature of coordinated metal ions affects the biological response. Molecular docking studies against DNA gyrase (PDB:4Z2C) revealed favorable binding affinities for the metal complexes compared to the free ligand suggesting a possible influence of metal coordination on protein interactions. Future work may focus on detailed in vivo studies to evaluate their pharmacological efficiency and toxicity profiles. Additionally, further investigations on structure–activity relationships (SAR) and modification of ligand frameworks could enhance their biological performance. Expanding computational studies, including advanced molecular dynamics simulations, may also provide deeper insight into their interaction mechanisms with biological targets.

CRediT authorship contribution statement

Eldeeb Marwa Huissen: Investigation, Funding acquisition, Formal analysis, Data curation, Conceptualization. **Elasala Gehan shabaan:** Conceptualization. **Rana M. Atta:** Conceptualization. **Ali Alaa eldin:**

Conceptualization. **Y. Sh. Mahrouse:** Conceptualization.

Declaration of Competing Interest

There are no financial or personal relationships that could inappropriately influence the work reported in this paper.

Appendix A. Supporting information

Supplementary data associated with this article can be found in the online version at doi:10.1016/j.nxmate.2026.102149.

References

[1] M. Trucksis, D.C. Hooper, J.S. Wolfson, Emerging resistance to fluoroquinolones in staphylococci: an alert, Ann. Intern. Med. 114 (1991) 424–426, https://doi.org/10.7326/0003-4819-114-5-424.

[2] D.T.W. Chu, P.B. Fernandes, Structure–activity relationships of the fluoroquinolones, Antimicrob. Agents Chemother. 33 (1989) 131–135, https://doi.org/10.1128/AAC.33.2.131.

[3] D.C. Hooper, J.S. Wolfson, Mode of action of the quinolone antimicrobial agents, Rev. Infect. Dis. 11 (1989) S902–S911, https://doi.org/10.1093/clinids/11.supplement_5.s902.

[4] J.S. Wolfson, D.C. Hooper, Bacterial resistance to quinolones: mechanisms and clinical importance, Rev. Infect. Dis. 11 (1989) S960–S968, https://doi.org/10.1093/clinids/11.Supplement_5.S960.

[5] J.M. Nelson, T.M. Chiller, J.H. Powers, F.J. Angulo, Fluoroquinolone-resistant Campylobacter species and the withdrawal of fluoroquinolones from use in poultry, Clin. Infect. Dis. 44 (2007) 977–980, https://doi.org/10.1086/512369.

[6] S. Kawahara, Chemotherapeutic agents under study, Nihon Rinsho J. Clin. Med. 56 (1998) 3096–3099.

[7] A. Mahmood, The efficacy of quinolones and fluoroquinolones in the medicine: a review study, Iraqi J. Med. Health Sci. 1 (2024) 27–35, https://doi.org/10.51173/ijmhs.v1i1.17.

[8] European Medicines Agency, Disabling and potentially permanent side effects of quinolone and fluoroquinolone antibiotics, EMA Report, 2019.

[9] P.G. Francis, R.J. Wells, Flumequine". Joint FAO/WHO Expert Committee on Food Additives. Residues of some veterinary drugs in animals and foods, FAO, Rome, 1998. ISBN 92-5-103061 -8.

[10] A. Tarushi, J. Kljun, I. Turel, A.A. Pantazaki, G. Psomas, D.P. Kessissoglou, Zinc(II) complexes with the quinolone antibacterial drug flumequine: Structure, DNA- and albumin-binding, N. J. Chem. 37 (2013) 342–355, https://doi.org/10.1039/c2nj40798a.

[11] K.C. Skyrianou, F. Perdih, I. Turel, D.P. Kessissoglou, G. Psomas, Nickel(II) complexes of the antibacterial drug flumequine: Interaction with DNA and albumin, J. Inorg. Biochem 104 (2010) 740–749, https://doi.org/10.1016/j.jinorgbio.2010.03.007.

[12] A. Barmpa, O. Frousiou, S. Kalogiannis, F. Perdih, I. Turel, G. Psomas, Manganese (II) complexes of flumequine: structure, antimicrobial activity and interaction with biomolecules, Polyhedron 151 (2018) 138–147, https://doi.org/10.1016/j.poly.2018.02.006.

[13] S.H. Iftikhar, S.R. Gilani, M.B. Taj, A. Raheel, et al., Design, synthesis and biological evaluation of organotin(IV) complexes of flumequine, J. Serb. Chem. Soc. 83 (2018) 425–437, https://doi.org/10.2298/JSC161203070I.

[14] A. A. El-Habeeb, M. Y. El-Sayed, I. M.A. Alatawy, M. S. Refat, Preparation, spectroscopic and anticancer investigations of metal–drug complexes of flumequine with La(III), Sm(III) and Tb(III) chloride, Bull. Chem. Soc. Ethiop. 38 (2024) 671–684, https://doi.org/10.4314/bcse.v38i3.10.

[15] M.S. Refat, Synthesis and characterization of ligational behavior of curcumin drug towards some transition metal ions, Spectrochim. Acta A 105 (2013) 326–337, https://doi.org/10.1016/j.saa.2012.12.041.

[16] A.I. Vogel, A Textbook of Quantitative Inorganic Analysis, Longmans, London, 1989.

[17] K. Nakamoto. Infrared Spectra of Inorganic and Coordination Compounds, 2nd ed., Wiley, New York, 2008 https://doi.org/10.1002/9780470405840.ch2.

[18] L.J. Bellamy, The Infrared Spectra of Complex Molecules, Chapman and Hall, London, 1975, https://doi.org/10.1007/978-94-011-6017-9.

[19] T.S. Britton, Hydrogen Ions, Chapman and Hall, London, 1955, https://doi.org/10.1002/ange.19560681740.

[20] B.D. Cullity, Elements of X-ray Diffraction, Addison-Wesley, Reading, MA, 1972, p. 102, https://doi.org/10.1107/S0567739479000917.

[21] M. Salavati-Niasari, F. Mohandes, F. Davar, M. Mazaheri, M. Monemzadeh, N. Yavarinia, Preparation of NiO nanoparticles from metal–organic frameworks, Inorg. Chim. Acta 362 (2009) 3691–3697, https://doi.org/10.1016/j.ica.2009.04.025.

[22] G. Carotenuto, F. Nicolais, Reversible thermochromic nanocomposites based on thiolate-capped silver nanoparticles, Materials 2 (2009) 1323–1340, https://doi.org/10.3390/ma2031323.

[23] J.W. Foster, H.B. Woodruff, Microbiological Aspects of Penicillin: VI. Procedure for the Cup Assay for Penicillin, J. Bacteriol. 47 (1944) 43–58, https://doi.org/10.1128/jb.47.1.43-58.1944.

[24] R.E. Miller, S.B. Rose, Studies with the Agar Cup-Plate Method: III. The Influence of Agar on Mercury Antiseptics, J. Bacteriol. 38 (1939) 539–547, https://doi.org/10.1128/jb.38.5.539-547.1939.

[25] J. Eberhardt, D. Santos-Martins, A.F. Tillack, S. Forli, AutoDock Vina 1.2.0, J. Chem. Inf. Model 61 (2021) 3891–3898, https://doi.org/10.1021/acs.jcim.1c00203.

[26] C.-H. Chu, K.-M. Li, S.-W. Lin, Crystal structure of starch binding domain, Proteins 82 (2014) 1079–1085, https://doi.org/10.1002/prot.24446.

[27] A.S. Waheeb, M.A. Awad, H.A.K. Kyhoiesh, A.M. Kadhum, J.A. Thabit, S.A. Lazam, Synthesis and characterization of Ni(II) and Cu(II) metal complexes containing new azo dye ligand (N,N,N) and evaluation of their biological activities supported by DFT studies, molecular docking, ADMET profiling, drug-likeness analysis and toxicity prediction, J. Mol. Struct. 1321 (2025) 139867, https://doi.org/10.1016/j.molstruc.2024.139867.

[28] A.M. Taher, et al., Synthesis, characterization, biological activity, and molecular docking studies of transition metal complexes derived from azo dye ligand, Results Chem. (2024) 101911, https://doi.org/10.1016/j.rechem.2024.101911.

[29] M.T. Rehman, M.F. AlAjmi, A. Hussain, Natural compounds as inhibitors of SARS-CoV-2, Curr. Pharm. Des. 27 (2021) 3577–3589, https://doi.org/10.2174/1381612826999201116195851.

[30] N.M. O'Boyle, M. Banck, C.A. James, Open Babel: an open chemical toolbox, J. Chemin.-. 3 (2011) 33, https://doi.org/10.1186/1758-2946-3-33.

[31] S. Dallakyan, PyRx – Python prescription v0.8, Scripps Research Institute, La Jolla, CA, 2008.

[32] R. Richards, H. Thompson, Vibrational spectra of phenolic deri-ati-es and phenolic resins, J. Chem. Soc. (1947) 1260–1269, https://doi.org/10.1039/JR9470001260.

[33] M.S. Masoud, A.E. Ali, M.A. Shaker, G.S. Elasala, Spectral study of metal complexes, Spectrochim. Acta A 90 (2012) 93–100, https://doi.org/10.1016/j.saa.2012.01.028.

[34] H. Zegota, M. Koprowski, A. Zegota, Effect of irradiation, Radiat. Phys. Chem. 43 (1994) 343–350, https://doi.org/10.1016/0969-806X(94)90024-8.

[35] M.G.Abd El-Wahed, M.S. Refat, S.M. El-Megharbel, Bull. Mater. Sci. 32 (2009) 205–212, https://doi.org/10.1007/s12034-009-0032-x.

[36] F.A.I. Al-Khodir, M.S. Refat, Synthesis, structural characterization and biological studies of some nalidixic acid–metal complexes: metalloantibiotic complexes of some divalent and trivalent metal ions, J. Mol. Struct. 1094 (2015) 22–35, https://doi.org/10.1016/j.molstruc.2015.03.063.

[37] A.A. Almehizia, M.A. Al-Omar, A.M. Naglah, M.A. Bhat, F.S. Alanazi, F.A. Alotaibi, M.S. Refat, A.M.A. Adam, Complexes of the antibiotic drug oxolinic acid with Fe (III), Zn(II), Ca(II), and Mg(II) ions: preparation, characterization, and in vitro evaluation of biological activity, Crystals 13 (2023) 1012, https://doi.org/10.3390/cryst13071012.

[38] A. Tarushi, P. Christofis, G. Psomas, Synthesis, characterization and interaction with DNA of mononuclear metal complexes with oxolinic acid, Polyhedron 26 (2007) 3963–3972, https://doi.org/10.1016/j.poly.2007.04.031.

[39] R.L. Carlin, M.J. Baker, J. Chem. Soc. (1964) 5008–5014, https://doi.org/10.1039/JR9640005008.

[40] R. Atkins, G. Brewer, E. Kokot, G.M. Mockler, E. Sinn, Inorg. Chem. 24 (1985) 127–134, https://doi.org/10.1021/ic00196a003.

[41] C.R. Krishnamoorthy, M.M. Taqui Khan, J. Coord. Chem. 12 (1983) 313–320, https://doi.org/10.1080/00958978308073864.

[42] M.B.H. Howlader, M.S. Islam, M.R. Karim, J. Chem. 39A (2000) 407–412, https://doi.org/10.1093/jb/mvz077.

[43] A. Sreekanth, M. Joseph, H.K. Fun, M.R.P. Kurup, Formation of manganese (II) complexes of substituted thiosemicarbazones derived from 2-benzoylpyridine: structural and spectroscopic studies, Polyhedron 25 (2006) 1408–1414, https://doi.org/10.1016/j.poly.2005.10.004.

[44] R.S. Drago, Physical Methods in Chemistry, Reinhold, New York, 1965, https://doi.org/10.1007/978-3-642-67117-3_8.

[45] F.A.I. Al-Khodir, M.S. Refat, Synthesis, structural characterization and biological studies of some nalidixic acid–metal complexes: metalloantibiotic complexes of some divalent and trivalent metal ions, J. Mol. Struct. 1094 (2015) 22–35, https://doi.org/10.1016/j.molstruc.2015.03.063.

[46] N.G. Yernale, B.S. Mathada, O. Anjaneyulu, N. Basamma, N.D. Sudharani, P. Kaveri, P. Karunakar, P. Chidre, H.M. Navya, Harnessing the therapeutic potential of macromolecular metal(II) complexes derived from quinoline and thiazole ligands, J. Mol. Struct. 1338 (2025) 142280, https://doi.org/10.1016/j.molstruc.2025.142280.

[47] S.M.H. Obaid, A.E. Abd-Almonuim, H.A.S. Al-Naymi, A.J. Jarad, M.M. Saleh, Synthesis and characterization of some metal ion complexes with mixed ligand of azo dye and metformin and evaluation of their biological activity, Heliyon 10 (2024) e37849, https://doi.org/10.1016/j.heliyon.2024.e37849.

[48] a) N.G. Yernale, B.S. Matada, G.B. Vibhutimath, V.D. Biradar, M.R. Karekal, M. D. Udayagiri, M.B. Hire Mathada, Indole core-based copper(II), cobalt(II), nickel (II) and zinc(II) complexes: synthesis, spectral and biological study, J. Mol. Struct. 1248 (2022) 131410;
b) K. Laarej, M. Bouachrine, S. Radi, S. Kertit, B. Hammouti, J. Chem. Sci. 7 (2010) 419–131427, https://doi.org/10.1155/2010/273206.

[49] K. Laarej, M. Bouachrine, S. Radi, S. Kertit, B. Hammouti, J. Chem. Sci. 7 (2010) 419–427, https://doi.org/10.1155/2010/273206.

[50] N. Raman, A. Kulandaisamy, C. Thangaraja, Transit. Met. Chem. 29 (2004) 129–134, https://doi.org/10.1023/B:TMCH.0000019409.50574.0a.

[51] M.B.H. Howlader, M.S. Islam, M.R. Karim, J. Chem. 39A (2000) 407–412, https://doi.org/10.1093/jb/mvz077.

[52] D. Thorburn-Burns, J. Bassett, R.C. Denney, G.H. Jeffery, J. Mendham, Vogel's Textbook of Quantitative Inorganic Analysis, Longman, 1978.

[53] M.S. Masoud, A. El-Marghany, A. Orabi, A.E. Ali, R. Sayed, Spectrochim. Acta A 107 (2013) 179–187, https://doi.org/10.1016/j.saa.2013.01.022.
[54] M.S. Masoud, G.B. Mohamed, Y.H. Abdul-Razek, A.E. Ali, Spectrosc. Lett. 35 (2002) 377–413, https://doi.org/10.1081/SL-120005674.
[55] M.S. Masoud, A.E. Ali, H.M. Ahmed, E.A. Mohamed, J. Mol. Struct. 1050 (2013) 43–52, https://doi.org/10.1016/j.molstruc.2013.07.020.
[56] M.S. Masoud, A.E. Ali, G.S. Elasala, E.A. Mohamed, S.A. Kolkaila, Heliyon 5 (2019) e02912, https://doi.org/10.1016/j.heliyon.2019.e02912.
[57] M. Banyay, M. Sarkar, A. Gräslund, Biophys. Chem. 104 (2003) 477–488, https://doi.org/10.1016/s0301-4622(03)00035-8.
[58] V. Bloomfield, D. Crothers, I. Tinoco, Nucleic Acids: Structures, Properties and Functions, University Science Books, 2000.
[59] C.K. Chu, Recent advances in nucleosides, Chemotherapy 505 (2002).
[60] H.E. Kissinger, Reaction kinetics, Anal. Chem. 29 (1957) 1702–1706, https://doi.org/10.1021/ac60131a045.
[61] M. Zare-Gachi, H. Daemi, J. Mohammadi, Mater. Sci. Eng. C. 107 (2020) 110321, https://doi.org/10.1016/j.msec.2019.110321.
[62] H.H. Hammud, K.T. Holman, M.S. Masoud, A. El-Faham, H. Beidas, Inorg. Chim. Acta 362 (2009) 3526–3532, https://doi.org/10.1016/j.ica.2009.03.046.
[63] M.F. Dehnayebi, G.M. Ziarani, T.N. Lohith, S. Ghareghomi, Z. Panahande, M. Farsadrooh, M. Majidinia, Probing the biological activity of isatin derivatives against human lung cancer A549 cells: Cytotoxicity, CT-DNA/BSA binding, DFT/TD-DFT, topology, ADME-Tox, docking and dynamic simulations, J. Mol. Liq. 428 (2025) 127475, https://doi.org/10.1016/j.molliq.2025.127475.
[64] M.S. Masoud, S.S. Hagagg, A.E. Ali, N.M. Nasr, Synthesis and spectroscopic characterization of gallic acid and some of its azo complexes, J. Mol. Struct. 1014 (2012) 17–25, https://doi.org/10.1016/j.molstruc.2012.01.041.
[65] R. Nalini, S.M. Basavarajaiah, G.Y. Nagesh, J. Mohammad, K. Ramakrishna Reddy, Synthesis, characterization, DFT analysis, biological evaluation, and molecular docking of Schiff base derived from isatin–isoniazid and its metal(II) complexes, Polycycl. Aromat. Compd. 43 (2023) 7597–7614, https://doi.org/10.1080/10406638.2022.2138927.
[66] N.G. Yernale, B.S. Mathada, S. Shivprasad, S. Hiremath, P. Karunakar, A. Venkatesulu, Spectroscopic, theoretical and computational investigations of novel benzo[b]thiophene-based ligand and its M(II) complexes as potential antimicrobial and antioxidant agents, Spectrochim. Acta A 302 (2023) 123114, https://doi.org/10.1016/j.saa.2023.123114.
[67] I. Laponogov, X.-S. Pan, D.A. Veselkov, K.E. McAuley, L.M. Fisher, M.R. Sanderson, Structural insight into the quinolone–DNA cleavage complex of type IIA topoisomerases, Acta Crystallogr. D. Struct. Biol. 72 (2016) 173–182, https://doi.org/10.1107/S2059798316001212.
[68] N.G. Bush, K. Evans-Roberts, A. Maxwell, DNA topoisomerases, EcoSal 6 (2015), https://doi.org/10.1128/ecosalplus.ESP-0010-2014.
[69] F. Collin, S. Karkare, A. Maxwell, Exploiting bacterial DNA gyrase as a drug target: current state and perspectives, Appl. Microbiol. Biotechnol. 92 (2011) 479–497, https://doi.org/10.1007/s00253-011-3557-z.
[70] H.A.K. Kyhoiesh, K.J. Al-Adilee, Pt(IV) and Au(III) complexes with tridentate benzothiazole-based ligand: Synthesis, characterization, biological applications and molecular docking and DFT calculation, Inorg. Chim. Acta 555 (2023) 121598, https://doi.org/10.1016/j.ica.2023.121598.
[71] H.A.K. Kyhoiesh, H.M. Hassan, Synthesis, characterization, in silico DFT, molecular docking, ADMET profiling studies and toxicity predictions of Ag(I) complex derived from 4-aminoacetophenone, ChemistrySelect (2024), https://doi.org/10.1002/slct.202304429.